Draft version October 28, 2016
Preprint typeset using LaTeX style emulateapj v. 01/23/15

arXiv:1603.01622v2 [astro-ph.GA] 27 Oct 2016

X-RAY DETECTED ACTIVE GALACTIC NUCLEI IN DWARF GALAXIES AT $0 < z < 1$

K. Pardo[1,*], A. D. Goulding[1], J. E. Greene[1], R.S. Somerville[2], E. Gallo[3], R.C. Hickox[4], B.P. Miller[5], A.E. Reines[6,†], & J.D. Silverman[7]

[1] Department of Astrophysical Sciences, Princeton University, 4 Ivy Lane, Princeton, NJ 08544, USA; kpardo@astro.princeton.edu
[2] Department of Physics and Astronomy, Rutgers University, 136 Frelinghuysen Road, Piscataway, NJ 08854, USA
[3] Department of Astronomy, University of Michigan, 1085 South University Avenue, Ann Arbor, MI 48109, USA; Hubble Fellow
[4] Department of Physics and Astronomy, Dartmouth College, 6127 Wilder Laboratory, Hanover, NH 03755, USA
[5] Department of Chemistry and Physical Sciences, The College of St. Scholastica, Duluth, MN 55811, USA
[6] National Optical Astronomy Observatory, 950 North Cherry Avenue, Tucson, AZ 85719, USA and
[7] Kavli Institute for the Physics and Mathematics of the Universe (WPI), The University of Tokyo Institutes for Advanced Study, The University of Tokyo, Kashiwa, Chiba 277-8583, Japan

Draft version October 28, 2016

ABSTRACT

We present a sample of accreting supermassive black holes (SMBHs) in dwarf galaxies at $z < 1$. We identify dwarf galaxies in the NEWFIRM Medium Band Survey with stellar masses $M_\star < 3 \times 10^9 M_\odot$ that have spectroscopic redshifts from the DEEP2 survey and lie within the region covered by deep (flux limit of $\sim 5 \times 10^{-17} - 6 \times 10^{-16}$erg cm^{-2} s^{-1}) archival *Chandra* X-ray data. From our sample of 605 dwarf galaxies, 10 exhibit X-ray emission consistent with that arising from AGN activity. If black hole mass scales roughly with stellar mass, then we expect that these AGN are powered by SMBHs with masses of $\sim 10^5 - 10^6$ $M_\odot$ and typical Eddington ratios $\sim 5\%$. Furthermore, we find an AGN fraction consistent with extrapolations of other searches of $\sim 0.6-3\%$ for 10^9 $M_\odot \leq M_\star \leq 3 \times 10^9$ $M_\odot$ and $0.1 < z < 0.6$. Our AGN fraction is in good agreement with a semi-analytic model, suggesting that as we search larger volumes we may use comparisons between observed AGN fractions and models to understand seeding mechanisms in the early universe.

Subject headings:

1. INTRODUCTION

Supermassive black holes (SMBHs; median mass of 10^8 $M_\odot$) are ubiquitous in massive, bulge-dominated galaxies (e.g. Kauffmann et al. 2003a), and the masses of these black holes have been found to correlate with the properties of the stellar spheroid (e.g., the galaxies' stellar velocity dispersion, $M_{\rm BH} - \sigma_\star$; e.g., McConnell et al. 2012; Kormendy & Ho 2013). These relationships suggest that a full understanding of galaxy evolution requires knowledge of SMBH formation and evolution. Unfortunately, there is very little known about SMBH formation and detecting the first SMBHs directly is practically impossible with the tools currently available.

Low-mass SMBHs ($M_{\rm BH} \leq 10^6$ $M_\odot$) in dwarf galaxies ($M_\star \leq 3 \times 10^9$ $M_\odot$, or approximately the mass of the Large Magellanic Cloud), which are expected to have had little growth through mergers or accretion, can provide an indirect window onto the primordial seeds of the SMBHs in the more massive galaxies we see today (Bellovary et al. 2011). Therefore, the distribution of central black hole masses in dwarf galaxies can give us many insights into SMBH and galaxy evolution (see reviews in Volonteri 2010; Greene 2012).

It is unclear whether all dwarf galaxies harbor massive black holes. From dynamical measurements, it is believed that M33 must have a supermassive black hole no larger than 1500 $M_\odot$, if it has one at all (Gebhardt et al. 2001). Likewise, any black hole in NGC 205 must be less than 3.8×10^4 $M_\odot$ (Valluri et al. 2005). On the other hand, there is dynamical evidence for SMBHs in some nearby dwarf galaxies, such as NGC404 and NGC 4395, which appear to host black holes with masses $\sim 10^5$ $M_\odot$ (see, for example, Filippenko & Sargent 1989; Seth et al. 2010; Thornton et al. 2008; den Brok et al. 2015). In order to understand the connection between SMBHs and dwarf galaxies, we need a large, representative sample of dwarf galaxies with central SMBHs.

With current technology, direct dynamical measurements of $< 10^5$ $M_\odot$ black holes cannot extend beyond a few Mpc. On the other hand, accreting SMBHs, known as active galactic nuclei (AGN), can be identified up to very large redshifts. The first attempts to search for a large sample of AGN in dwarf galaxies used broad and/or narrow optical emission lines to find AGN (e.g. Greene & Ho 2004, 2007; Dong et al. 2012; Reines et al. 2013; Moran et al. 2014). However, optical data is inherently limited by dust obscuration and emission from star formation (Goulding & Alexander 2009). Both mid-IR (Satyapal et al. 2008, 2009; Sartori et al. 2015) and radio (Reines et al. 2011, 2014) searches have yielded complementary samples for follow-up (Whalen et al. 2015; Reines & Deller 2012). In this paper, we focus on X-rays, which are insensitive to obscuration by dust and provide a relatively clean tool for identifying accreting black holes (e.g., Brandt & Alexander 2015). Searches of local dwarf galaxies in the X-ray have also yielded interesting targets (Desroches & Ho 2009; Schramm et al. 2013; Lemons et al. 2015). Miller et al. (2015) used a uniform survey of early-type galaxies within 30 Mpc to constrain the distribution of black hole masses in dwarf galaxies, but were fundamentally limited by their very small volume.

In order to find the best estimate of the occupation

* kpardo@astro.princeton.edu
† Hubble Fellow

fraction of SMBHs in dwarf galaxies, larger survey volumes must be used, which implies we must push to higher redshifts. Recent deep surveys now allow us to complete a search for SMBHs in dwarf galaxies up to $z \sim 1$. X-ray stacking has been used to search for dwarf galaxies up to $z < 1.5$ (Mezcua et al. 2016), but using the technique of looking for X-ray point sources that correspond to dwarf galaxies beyond $z \sim 0.4$ has not yet been attempted. Searching for X-ray point sources that coincide with dwarf galaxies at these higher redshifts requires deep X-ray data, as well as accurate galaxy masses in the same region.

We have performed a search for SMBHs in dwarf galaxies up to redshift $z \lesssim 1$ in order to shed light on SMBH and galaxy evolution. In this paper, we outline our search for SMBHs in dwarf galaxies identified using a combination of NEWFIRM Medium-Band Survey (NMBS), *Hubble Space Telescope* (*HST*), *Chandra* X-ray Observatory, & DEEP2 observations. In Section 2, we outline our source selection process. We begin by identifying dwarf galaxies ($M_\star < 3 \times 10^9\ M_\odot$) with DEEP2 spectroscopic redshifts $z < 1$ in the AEGIS field using the NMBS. We then analyze these sources using *Chandra* X-ray Observatory archival data. Section 3 details the results of our search, while Section 4 discusses the Eddington and AGN fractions that we measure and how these results compare to other studies and simulations. Section 5 is a summary. Throughout, we assume the standard, flat ΛCDM cosmology with parameters: $H_0 = 68$ km s^{-1} Mpc^{-1} and $\Omega_m = 0.3$.

2. DATA & SOURCE SELECTION

Our goal is to select dwarf galaxies ($M_\star \leq 3\times10^9\ M_\odot$) that may harbor central SMBHs. For this, we require deep X-ray data and complementary multi-wavelength data that can provide estimates of the galaxy properties. In addition, it is important to have deep, homogenous spectroscopic redshifts and high spatial resolution imaging. The All-Wavelength Extended Groth Strip International Survey (AEGIS) field has deep X-ray data ($\sim 200 - 800$ ks) while still providing sufficient volume for statistically significant source numbers and excellent multi-wavelength data. The AEGIS field is centered at $\alpha = 14^{\rm h}17^{\rm m}$, $\delta = +52°30^{\rm m}$ (J2000), and covers an area of ~ 0.9 deg^2 (Davis et al. 2002; Davis et al. 2007). The requirement of data from the NMBS, *HST* and *Chandra* within the AEGIS field yields a contiguous overlapping footprint of ~ 0.1 deg^2 (see Figure 1). We select galaxies within this region as described below.

2.1. *A Dwarf Galaxy Sample with Robust Stellar Mass Measurements*

For reliable stellar masses, we turn to the NEWFIRM Medium-Band Survey (NMBS; see Whitaker et al. 2011, for a complete description), which is a near-infrared imaging survey of part of the AEGIS field. Since this survey splits the broad-band JHK bands into 7 medium-band filters, there is improved modeling of the spectral energy distribution, which leads to more dependable stellar masses (van Dokkum et al. 2009). The $27'.6 \times 27'.6$ NMBS survey region is centered at $\alpha = 14^{\rm h}18^{\rm m}00^{\rm s}$, $\delta = +52°36^{\rm m}07^{\rm s}$ (J2000) (van Dokkum et al. 2009). The K-band 90% limiting magnitude is 22.5 AB mag and the

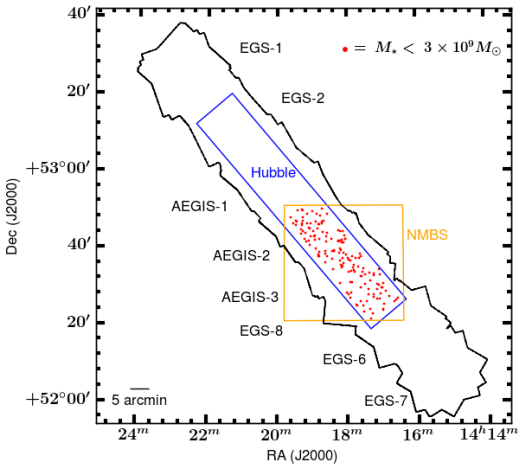

FIG. 1.— Survey region with galaxies selected from the NEWFIRM Medium-Band Survey (NMBS) indicated. The black line outlines the *Chandra* X-ray Observatory AEGIS observations. The blue line corresponds to the *Hubble Space Telescope* observations, and the yellow line shows the region covered by the NMBS. The red circles indicate the positions of the low-mass ($M_\star < 3 \times 10^9 M_\odot$) galaxies with DEEP2 spectroscopic redshifts $z < 1$ selected from the NMBS.

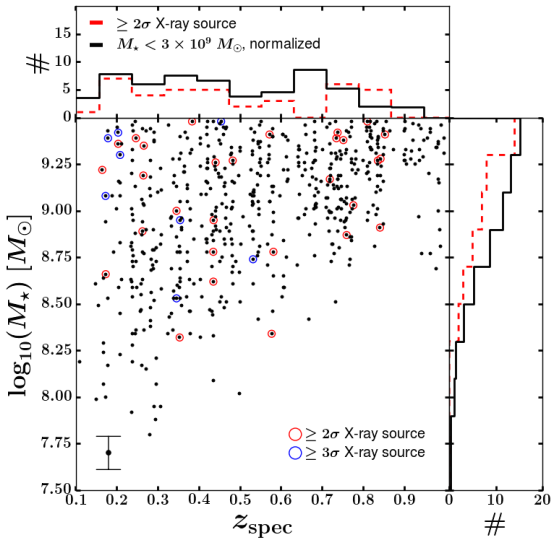

FIG. 2.— Stellar Mass as a function of redshift, with mass and redshift histograms for the dwarf galaxies selected from the NMBS. The black points and lines indicate all dwarf galaxies selected from the NMBS, with the histograms normalized to 10% of their actual values to enable better comparison with the $\geq 2\sigma$ X-ray sources. The red circles and red dotted lines indicate our $\geq 2\sigma$ X-ray sources. The blue circles signify our $\geq 3\sigma$ X-ray sources.

50% limiting magnitude is 23.6 AB mag (Whitaker et al. 2011). The NMBS sources were K-band selected using SExtractor (Bertin & Arnouts 1996), and the stellar population parameters, including star formation rates, were derived with FAST (Kriek et al. 2009) using the Bruzual & Charlot (2003) models and an exponentially declining star formation history. The Bruzual & Charlot (2003) models use the Chabrier (2003) initial mass function. To ensure more accurate stellar masses, the NMBS used spectroscopic redshifts from the DEEP2 survey, which has a limit of $R < 24.1$ mag, (Davis et al. 2002; Steidel et al. 2003) when available. For our purposes, accurate

stellar masses are paramount, hence we restrict ourselves to the sources with spectroscopic redshifts. In addition, we restrict the galaxies to those with $z_{spec} < 1$ to match the mass sensitivity of the NMBS. Of the 27652 sources identified by the NMBS, we find 642 within our mass and redshift ranges that have spectroscopic redshift measurements.

To ensure that all of our sources are dwarf galaxies rather than tidal tails mistakenly identified by the NMBS, we require morphologies of our sources. *HST* surveyed a 0.197 deg^2 region of the AEGIS field using the Advanced Camera for Surveys (ACS) (Davis et al. 2007). Using the *HST* data, we discard 37 of the galaxies within our mass and redshift ranges because they are mergers. We exclude these mergers because of the possibility of inaccurate mass measurements. This leaves us with 605 sources selected from the NMBS and *HST* data.

The 605 galaxies selected are shown, binned by mass and redshift, in Figure 2. The masses range from $\sim 5 \times 10^7$ $M_\odot$ to 3×10^9 $M_\odot$. The star formation rates (SFR) vary from $\sim 3 \times 10^{-4}$ to 10 $M_\odot$ yr^{-1}, with a median SFR $= 0.24$ $M_\odot$ yr^{-1}.

2.2. *X-ray Analysis*

We now identify the dwarf galaxies from our sample that show significant X-ray emission by using the available X-ray data within the AEGIS field. The *Chandra* X-ray Observatory has observed ~ 0.7 deg^2 of AEGIS with the Advanced CCD Imaging Spectrometer (ACIS) as part of XDEEP2 (Goulding et al. 2012, see also Nandra et al. 2005; Laird et al. 2009; Nandra et al. 2015). To ensure the most reliable measurements, we apply the latest calibration files using the CIAO software (version 4.7) and CALDB 4.6.5 (Fruscione et al. 2006).

Our X-ray analysis consists of performing forced aperture photometry at the optical positions of our selected galaxies. Some of our selected galaxies have X-ray data from different, overlapping subregions within AEGIS. However, we only use the X-ray data from the region with an aim-point closest to each source. This is because we wish to limit the amount of contamination from diffuse emission, and the *Chandra* point-spread function (PSF) deteriorates with distance from the aim-point. We define the X-ray source region as the 90% enclosed energy radius around the optical source position using the CIAO `psf` module. This is done for the soft band (SB; $0.5 - 2$ keV), the hard band (HB; $2 - 7$ keV), and the full band (FB; $0.5 - 7$ keV). The 90% enclosed energy radii range from $\sim 1'' - 15''$ for most of our sources. We define the background region to be a square with sides that are at least four times as large as the radius of the source region. We find that 23 of the 605 dwarf galaxies selected from the NMBS have a second spatially coincident galaxy within the 90% enclosed energy radius. The X-ray photons associated with these neighbors cannot be reliably disentangled from the target dwarf galaxy, and thus these 23 sources are discarded from the sample.

Note that our method here differs from that of traditional X-ray catalogs created independently of multi-wavelength source positions. Using X-ray data alone to detect a source necessitates a high cut in X-ray signal-to-noise. However, our forced photometry method allows us to identify X-ray sources that may fall below the typical significance level cut and helps to mitigate the effects of Eddington bias (see Gibson & Brandt 2012). Since we already know that there is an optical source at a given position, we can accept a lower level of significance and still expect almost no false positives from random background fluctuations. Assuming a false detection probability of 0.27% (a 3-sigma confidence limit), we expect only ~ 2 false positives from our 583 sources (605 sources minus 23 sources with contaminants). This approach is standard for deep field Spitzer data, and WISE catalog construction (e.g., Lang et al. 2014). In addition, a similar implementation has recently been performed on the CDF-S/N by Xue et al. (2016).

We determine the flux for each source using the same prescription followed in Goulding et al. (2012). A count rate to flux conversion is applied assuming a power law spectrum with a photon index of 1.9, and Galactic $N_{\rm H}$ $\sim 1 \times 10^{20}$ cm^{-2} (Kalberla et al. 2005). We calculate the X-ray luminosity for each of our sources using the DEEP2 spectroscopic redshifts, and bring each X-ray luminosity to the rest frame by K-correcting the luminosities using a typical power-law with $\Gamma = 1.9$ (Brandt & Hasinger 2005). Finally, we calculate the hardness ratios (HRs) for each of our sources, which is given by

$$HR = \frac{H - S}{H + S}\,, \tag{1}$$

where H is the number of HB counts and S is the number of SB counts. We use the Bayesian Estimation of Hardness Ratios code (Park et al. 2006) to calculate the HR and its associated uncertainties. HRs vary from -1 to 1, with typically more positive values for AGN and more negative values for X-rays produced by stellar processes (Brandt & Hasinger 2005).

For each of our sources, we compute a false detection probability, which gives the probability of a spurious X-ray source being falsely identified as a significant source. In order to compute the false detection probability, we assume that the number of background counts have a Poisson distribution with a mean equal to the number of counts observed in the background region normalized to the area of the source region for each source. We then sample from this distribution 10^6 times. The false detection probability is the percentage of times that the sampled distribution produced counts greater than the observed source counts. We calculate this probability for the SB, HB, and FB. The false detection probability is used to set the significance of our sources (i.e. a false detection probability $< 4.55\%$ denotes a $\geq 2\sigma$ source). We consider a source to be a $\geq 3\sigma$ or $\geq 2\sigma$ detection if it is significant to that level in any of the three bands. Given the effective area of the ACIS instrument, *Chandra* is most sensitive and has the smallest PSF at soft energies, where the background is also the lowest. In the low-number Poisson regime, there is a further trade-off that more robust detections can be made over the widest possible energy band. Thus, our false detection probabilities are assigned as follows: full-band, soft-band and hard-band. Note that the NMBS and *Chandra* astrometry is matched within $\sim 0\farcs9$ (Nandra et al. 2015), so we allow our $\geq 3\sigma$ X-ray centroid positions to vary by up to $1''$ before applying the counts to flux conversion.

3. RESULTS

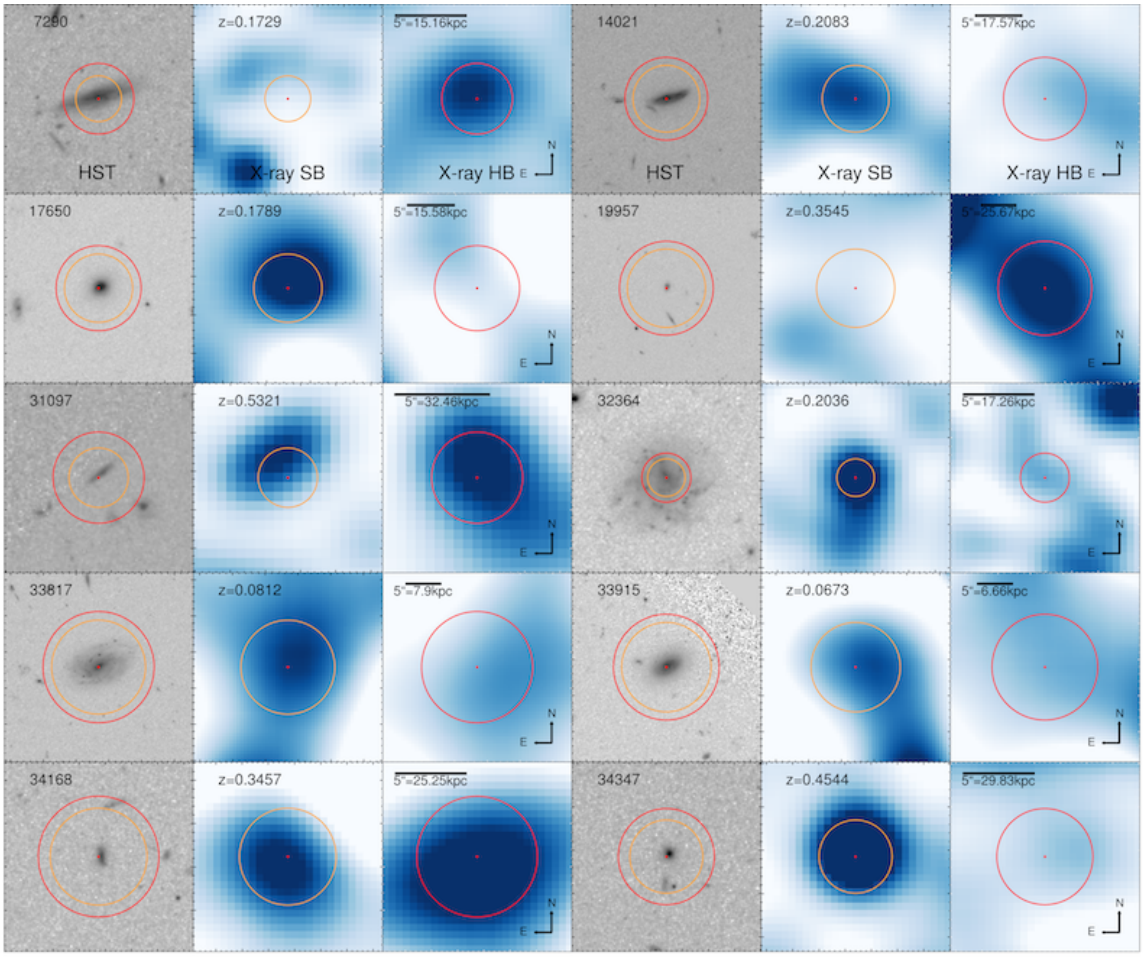

FIG. 3.— *Hubble Space Telescope*(left) images alongside *Chandra* X-ray Observatory soft-band (SB; 0.5 - 2 keV; center) and hard-band (HB; 2 - 7 keV; right) images of our $\geq 3\sigma$ objects. The red x's mark the galaxy position, while the 90% enclosed energy radii are shown in orange (SB) and red (HB).

There are 151 dwarf galaxies selected from the NMBS with X-ray fluxes above the detection threshold. As described in detail below, we find 10 sources with $\geq 3\sigma$ detections and 29 sources with $\geq 2\sigma$ significant detections (Section 3.1). We give the optical properties of our $\geq 2\sigma$ sources in Table 1, and their X-ray properties in Table 2. We discuss the nature of these X-ray sources in Section 3.2.

3.1. *X-ray Detections*

We consider any $\geq 3\sigma$ sources (those with false detection probability $< 0.27\%$) to be a robust X-ray detection. These ten sources are shown circled in blue in Figure 2 and their properties are given in Table 3. Their *HST* and *Chandra* X-ray Observatory images are given in Figure 3. Of the ten, seven are significant in the FB and one other band, two are only significant sources in the SB, one is only significant in the HB, and two sources are significant in all three bands. Note that the observed SB and HB correspond to rest-frame $0.75 - 3$ keV and $3 - 10$ keV, respectively at $z = 0.5$. The redshifts range from $z \approx 0.08 - 0.53$, although most of the sources are below $z \sim 0.3$. This could be due to the incompleteness of the DEEP2 spectra, which we discuss further in Section 4.2. The rest frame X-ray luminosities of these sources range from $L_{\rm X} \sim 4 \times 10^{39}$ erg s^{-1} to 2×10^{42} erg s^{-1}. The median hardness ratio for these sources is -0.09 and the median SFR is $\sim 0.3\ M_{\odot}$ yr^{-1}. Goulding et al. (2012) performed a blind X-ray search in the AEGIS field, and found three sources that correspond to galaxies in the NMBS within our stellar mass range. Two of those sources, 17650 and 34347, are also identified by our method. Our estimated $L_{\rm X}$ agrees with that from Goulding et al. (2012) for both sources. The final source they identified, 31041, was removed from our sample because it is a merging system.

Using the *HST* data, we can glean some basic information about the morphologies of our sources. Most are late-type spirals at a variety of inclinations (see Figure 3). However, one (19957) is irregular, and one at high redshift (34347) is compact with little else about its morphology readily identifiable. A more quantitative analysis of the morphologies (e.g., to determine their bulge-to-disk ratios) is beyond the scope of this paper.

Our $\geq 2\sigma$ sources (those with false detection probability $< 4.55\%$) are included as grey x's in Figures 4 and 5, and their properties are included in Tables 1 and 2. As described in Section 2.2, because our $\geq 2\sigma$ sources are at known galaxy positions, the vast majority are real sources. We include these sources as they enable us to

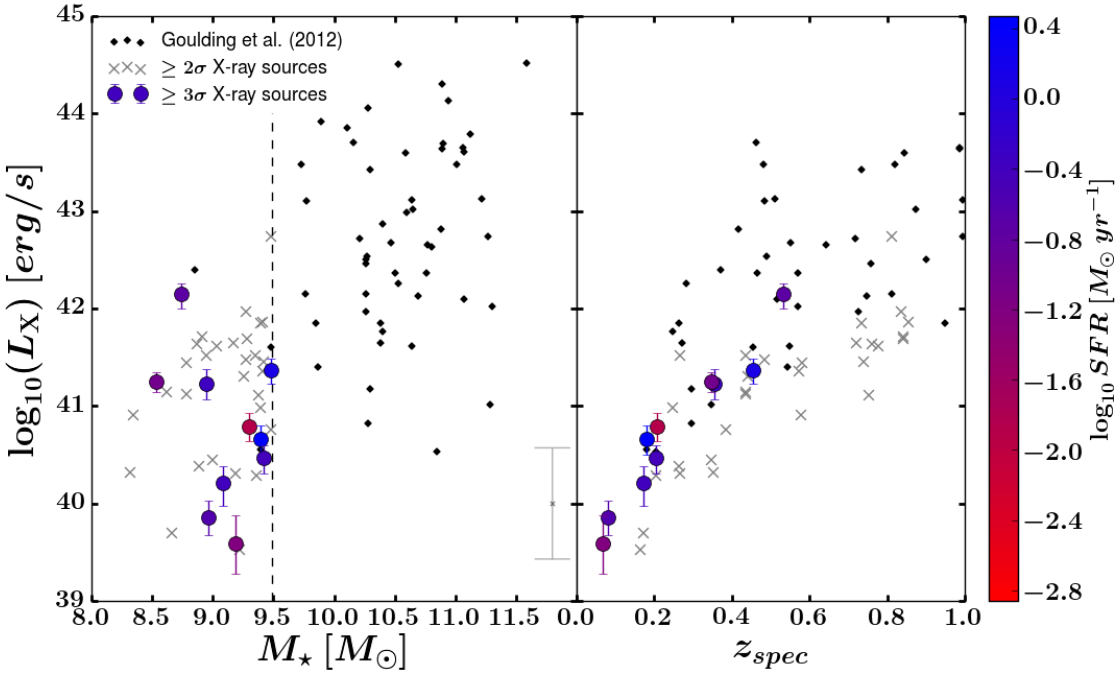

FIG. 4.— L_X as a function of $M_\star$ (*left*) and redshift (*right*) for our $\geq 3\sigma$ X-ray sources (colored points), $\geq 2\sigma$ X-ray sources (grey points), and sources found in Goulding et al. (2012) that correspond to galaxies in the NMBS (black points). The colors correspond to the SFR, as given by the NMBS. The black, dashed line shows our mass cut ($M_\star < 3 \times 10^9\ M_\odot$).

have a large enough sample to give better statistics on the AGN properties of our sample as a whole (Section 4).

3.2. *Nature of the X-ray Sources*

There are multiple processes that may produce X-ray emission in a star-forming galaxy other than SMBH accretion. High-mass X-ray binaries (HMXBs) are the dominant source of X-rays from star-forming regions (e.g. Fragos et al. 2013). Hot gas associated with supernovae remnants can also emit in the X-ray, although this should be a very small factor for such low star formation rates (see Mineo et al. 2012b). At $L_X > 10^{40}$ erg s^{-1}, HMXBs contribute many orders of magnitude more to the luminosity than the low-mass X-ray binaries (see, for example, Lehmer et al. 2010; Mineo et al. 2012a). Thus, we will mostly consider the contribution from HMXBs, but will also discuss LMXBs and X-ray emitting hot gas from supernovae remnants as AGN contaminants.

Although we cannot measure detailed X-ray spectra with so few counts, we can use hardness ratios as a proxy for the type of X-ray emission we are observing. Obscured AGN (intrinsic $N_H \gtrsim 1 \times 10^{22}$ cm^{-2}) normally have the highest hardness ratios of $HR > 0$, followed by unobscured AGN with $HR \sim -0.5$. HMXBs and X-ray emitting hot gas associated with supernovae remnants normally have very low hardness ratios of $HR \leq -0.8$ (Brandt & Hasinger 2005). The hardness ratios for our $\geq 2\sigma$ and $\geq 3\sigma$ sources are given in Tables 2 & 3, and plotted versus the spectroscopic redshift in Figure 5. We plot the expected hardness ratio as a function of redshift for an obscured AGN with $\Gamma = 1.9$ and intrinsic $N_H = 3 \times 10^{22}$ cm^{-2} (black, solid line), an unobscured AGN with $\Gamma = 1.9$ (blue, dashed line), an HMXB with

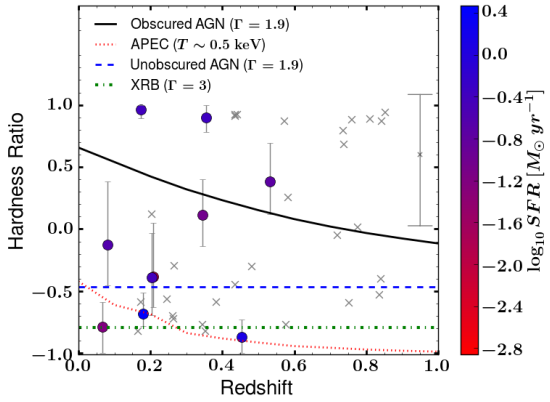

FIG. 5.— Hardness Ratio versus z for $\geq 2\sigma$ sources selected from the NMBS. The Hardness Ratio, $(H-S)/(H+S)$, is calculated using the Bayesian Estimation of Hardness Ratio Code. The colored points are all of the sources selected from the NMBS with $\geq 3\sigma$ X-ray detections, while the grey points indicate the $\geq 2\sigma$ X-ray sources. The colors correspond to the SFR, as given by the NMBS. The various lines give hardness ratios for different models as calculated by the PIMMS online calculator.

$\Gamma = 3$ (green, dotted-dashed line), and hot gas, for which we use the APEC model provided by Sherpa, at ~ 0.5 keV (red, dotted line). We calculate each of these with the PIMMS online calculator[3] and allow for a constant galactic $N_H = 1 \times 10^{20}$ cm^{-2}. As shown in the figure, three of our sources (7290, 19957, & 31097) are clearly obscured AGN as they fall well above the track shown for the model unobscured AGN. Most of our other sources are consistent with being either an obscured or unob-

[3] http://cxc.harvard.edu/toolkit/pimms.jsp

scured AGN. Our three softest sources (17650, 33915, & 34347) appear inconsistent with either AGN model. These low HRs could be consistent with AGN if these AGN were extremely obscured (e.g. reflection dominated X-ray spectra produced in the presence of Compton thick absorption). On the other hand, these HRs are consistent with the normal X-ray emission from star formation. This second scenario seems more likely for two of these sources (17650 & 34347) considering their SFRs of 0.47 $M_\odot$ yr^{-1} and 0.11 $M_\odot$ yr^{-1}, which are among the highest of our $\geq 3\sigma$ sources. Thus, based on HRs, we conclude that at least seven of our ten sources are likely AGN powered.

Now, we consider the possible contamination to the measured $L_{\rm X}$ due to HMXBs and LMXBs specifically. To quantify this contamination, we assign each source an X-ray binary (XRB) probability (i.e. the probability that the X-ray luminosity observed can be attributed to HMXBs or LMXBs). We assume Gaussian statistics, setting our mean to the observed X-ray luminosity in the full-band (FB), $L_{\rm X}$[4] and comparing it to the estimated X-ray luminosity due to XRBs, $L_{\rm XRB}$. We obtain $L_{\rm XRB}$ using the star formation rate (SFR) given by the NMBS and the relation given by Lehmer et al. (2010):

$$L_{\rm XRB} = \alpha M_\star + \beta SFR\,, \qquad (2)$$

where $\alpha = (9.05 \pm 0.37) \times 10^{28}$ erg s^{-1} M$_\odot^{-1}$ and $\beta = (1.62 \pm 0.22) \times 10^{39}$ erg s^{-1} (M$_\odot$/yr)$^{-1}$. This relation gives the luminosity in the $2-10$ keV energy range at redshift $z = 0$. However, at the typical redshift of our sources, rest-frame 2-10 keV corresponds to observed 0.3-7 keV, which is approximately our FB. The predicted $L_{\rm XRB}$ for each of our sources is given in Table 1. The 68% confidence interval for $L_{\rm XRB}$ of each of our sources is shown in Figure 6. The colored points are the measured $L_{\rm X}$ in the FB for each of our $\geq 3\sigma$ sources, where the colors correspond to the redshift. The grey points give the measured $L_{\rm X}$ in the FB for all of our $\geq 2\sigma$ sources. Eight of our $\geq 3\sigma$ sources are more than 3σ away from the expected $L_{\rm X}$ from star formation.

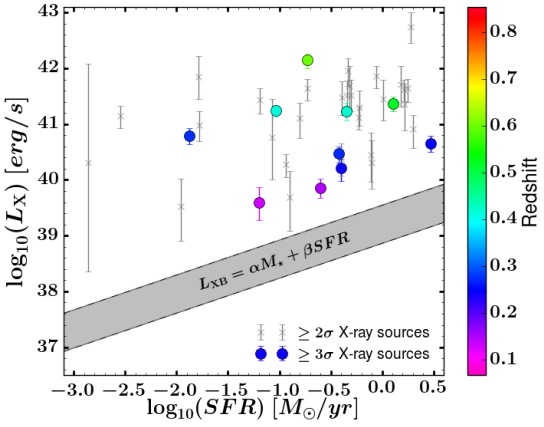

[4] The Gaussian we use is: $\frac{1}{\sigma\sqrt{2\pi}} e^{-\frac{1}{2}\left(\frac{x-\mu}{\sigma}\right)^2}$, where μ is the observed X-ray luminosity in the FB and σ is the error in our observed X-ray luminosity, which we calculate from the observed counts using Poisson statistics.

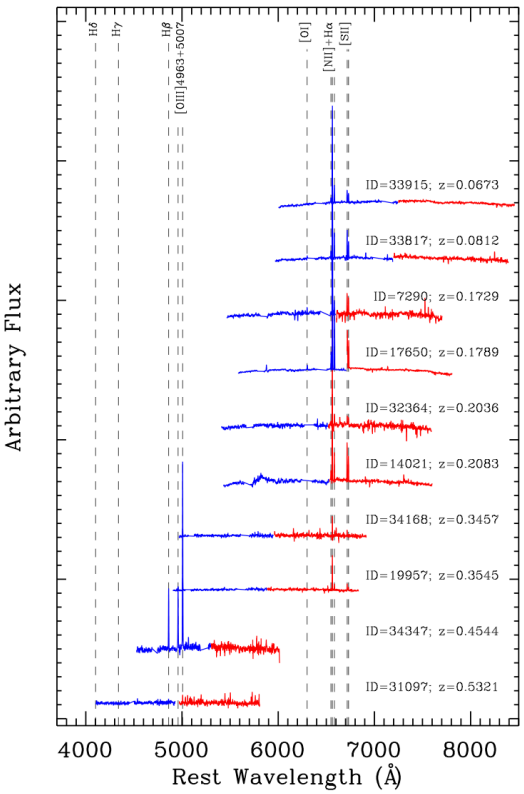

FIG. 7.— DEEP2 spectra with important emission lines marked for our $\geq 3\sigma$ X-ray sources. Note that object 31097 has no emission lines because the lines all fall in detector gaps.

FIG. 6.— X-ray luminosity as a function of star formation rate for the NMBS galaxies with $\geq 2\sigma$ X-ray detections. The shaded grey region indicates the 68% confidence interval for $L_{\rm XRB}$. The colored points represent the measured X-ray luminosity in the full-band for our $\geq 3\sigma$ sources. The colors correspond to the redshift of each source. The grey points correspond to our $\geq 2\sigma$ sources. Note that for most of these sources, $L_{\rm X,min}$ is still well above $L_{\rm XRB}$.

Since high-luminosity X-ray sources will only be populated stochastically at these SFRs $< 1 M_\odot$ yr^{-1} (Gilfanov et al. 2004), we also calculate the total number of luminous X-ray binaries expected in the entire sample, including any ultra-luminous X-ray sources (ULXs), which are X-ray sources with $L_{\rm X} > 10^{39}$ erg s^{-1} associated with star-forming regions. We take the summed SFR for our galaxies with $L_{\rm X} \geq 10^{40}$ erg s^{-1}, and integrate the best-fit power law for the luminosity distribution of the HMXBs given by Mineo et al. (2012a) over the range of luminosities we measured. We find that we should expect $\lesssim 3$ HMXBs/ULXs with $L_{\rm X} \geq 10^{40}$ erg s^{-1} in our entire sample. In line with our hardness ratio predictions, the distribution of $L_{\rm X}$ (given the SFRs in our sample) strongly suggests that at least seven of our ten sources are powered by AGN in the X-ray. We should stress that the X-ray binary luminosity function is still largely unknown - it is currently unclear how to include second order factors, like metallicity. There is some evidence that the X-ray binary luminosity function depends on metallicity, and is higher for metal-poor systems (Basu-Zych et al. 2016). However, this metallicity dependence is still not well known, so we do not attempt to correct for this effect here.

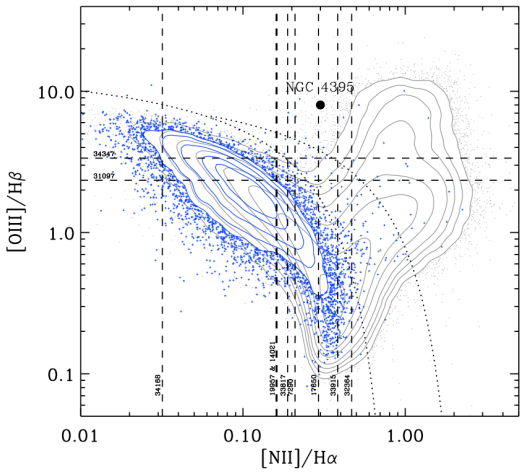

FIG. 8.— A Baldwin, Phillips & Terlevich (BPT) diagram (Baldwin et al. 1981). The dashed lines indicate the line ratios for our $\geq 3\sigma$ sources. The blue contours are given by all of the dwarf galaxies in SDSS, while the grey contours are all of the AGN in SDSS. The position of NGC 4395 is given as a reference. Note that our sources, as a whole, will most likely lie between the positions of the dwarf galaxies in SDSS and the AGNs in SDSS. The dotted lines give the boundary between starburst galaxies and AGN as found by Kauffmann et al. (2003b) (lower line) and Kewley et al. (2001) (upper line).

Another way of diagnosing the source of X-ray emission is to use the DEEP2 spectra to plot our sources on a Baldwin, Phillips & Terlevich (BPT) diagram (Baldwin et al. 1981). These diagrams use line ratios of strong optical emission lines to categorize the source of photoionization in galaxies. Normal star-forming galaxies occupy the left-hand locus of the BPT diagram (see Figure 8), with lower-metallicity sources typically having lower [N II]/Hα and higher [O III]/Hβ (e.g., Moustakas & Kennicutt 2006). AGN appear in the upper-right of the diagram, while AGN in dwarf galaxies, which also have low metallicity, tend to fall to the left of the typical AGN sequence due to their lower-than-average [N II]/Hα (e.g., NGC4395; Groves et al. 2006; Ludwig et al. 2009).

The DEEP2 spectra for our $\geq 3\sigma$ sources are given in Figure 7. With the exception of 31097, which was at the exact redshift where all of the necessary emission lines were in detector gaps, all of our sources exhibit strong [N II], [O III], Hα, or Hβ emission lines. Due to the coverage of DEEP2, none of the spectra include all of the lines needed to properly place the sources in a BPT diagram. However, we can consider the sample as an ensemble by plotting the ratios we do have for each source (either [N II]/Hα or [O III]/Hβ). The intersection of these lines places the sample in a spot on the BPT diagram ([N II]/H$\alpha \sim 0.15 - 0.35$, [O III]/H$\beta \sim 2 - 3$) between normal SDSS dwarf galaxies and AGN within SDSS (see Figure 8). This is consistent with the low-metallicity AGN described by Groves et al. (2006). Thus, the BPT diagram indirectly argues for AGN powering in our sources as well.

Therefore, the combination of hardness ratios, $L_{\rm X}$/SFR, and optical line ratios together strongly imply that our sample is dominated by AGN.

4. AGN PROPERTIES

As mentioned in Section 1, the SMBH occupation fraction in dwarf galaxies can be an important constraint on possible SMBH formation mechanisms. When we use accretion to find supermassive black holes, there is a natural degeneracy between the distribution of black hole mass and the distribution of accretion rates onto the black holes (e.g., Miller et al. 2015). It is well beyond the scope of this work to attempt to disentangle these two, but we do present active black hole fractions and compare with prior observational and theoretical work.

4.1. *Black Hole Masses & Eddington Ratios*

Eddington ratios are a useful tool for comparing AGN fractions from different studies; however, the masses of our black holes, $M_{\rm BH}$, are very uncertain. As mentioned in Section 1, we cannot measure the black hole masses $M_{\rm BH}$ using dynamical methods. We also cannot use the $M_{\rm BH} - \sigma_\star$ relation to infer $M_{\rm BH}$ because we do not have $\sigma_\star$ measurements. In addition, the $M_{\rm BH} - \sigma_\star$ relation has not been well-measured in this low-mass regime (e.g. Barth et al. 2004; Dong et al. 2012), and may not hold for late-type spiral galaxies (e.g. Greene et al. 2010).

For lack of more detailed data, we simply assume that $M_{\rm BH}$ scales with $M_\star$. This scaling is seen (e.g., Reines & Volonteri 2015), albeit with considerable scatter. To bracket this range, we take two extremes of the galaxy population at low mass: NGC 4395 and M32. NGC 4395 is a low-mass bulgeless spiral galaxy with a measured central SMBH mass of $M_{\rm BH} = 4^{+8}_{-3} \times 10^5 M_\odot$ (den Brok et al. 2015). M32 is a dwarf elliptical galaxy of a similar mass as NGC 4395, but with a measured central SMBH mass of $M_{\rm BH} = (2.4 \pm 1.0) \times 10^6 M_\odot$ (van den Bosch & de Zeeuw 2010). We use NGC 4395 and M32 to bracket the range of $M_{\rm BH}/M_\star$. For NGC 4395, $M_{\rm BH}/M_{\star,4395} = 3.5 \times 10^{-4}$ (Reines & Volonteri 2015), while for M32 this is $M_{\rm BH}/M_{\star,M32} = 8 \times 10^{-4}$ (van den Bosch & de Zeeuw 2010). We derive a corresponding average black hole mass range of $M_{\rm BH} \sim 5.5 \times 10^5 - 1.3 \times 10^6$ $M_\odot$ for both our $\geq 2\sigma$ and $\geq 3\sigma$ sources. To find the Eddington ratios, we assume that $L_{\rm X} = 0.1 \times L_{\rm bol}$ (Marconi et al. 2004). The range of average Eddington ratios, $L_{\rm bol}/L_{\rm Edd}$, for our $\geq 3\sigma$ sources is $3 - 7\%$, and $3 - 6\%$ for our $\geq 2\sigma$ sources.

4.2. *The Observed Fraction of AGN in Dwarf Galaxies*

This paper represents the first attempt to quantify the AGN fraction beyond $z \sim 0.4$ in $\sim 10^9$ $M_\odot$ galaxies. At the very least, the AGN fraction represents a lower limit on the fraction of dwarf galaxies that host massive black holes. As we will show, we are at the limits of the capabilities of both the optical and X-ray surveys, which makes quantifying our incompleteness challenging.

Let us start with our X-ray completeness. Examination of Figure 4 shows that for redshifts $0.2 < z < 0.8$, we are incomplete below an X-ray luminosity of $L_{\rm X} \sim 10^{41}$ erg s^{-1}. Thus, for calculating our AGN fraction we will only consider sources with $L_{\rm X}$ greater than this limit across our redshift range. Our optical limit, on the other hand, has a more complicated selection function. Our stellar masses are derived from the NMBS, whose point-source detection limit is $m_{\rm K} = 23.2$ AB. However, we also require a spectroscopic redshift from DEEP2, which introduces a known incompleteness for

faint red galaxies with $z > 0.7$ (Newman et al. 2013). We examine the ratio of the NMBS to DEEP2 sources in redshift bins, and find that this ratio remains constant out to $z \sim 0.8$ if we restrict our attention to galaxies with $M_\star > 10^9\ M_\odot$. However, to better compare with Aird et al. (2012) (see Section 4.3), we we will only consider up to $z < 0.6$. Thus, for calculating an AGN fraction, we also restrict our attention to a mass and redshift range of $10^9\ M_\odot \leq M_\star \leq 3 \times 10^9\ M_\odot$ and $0.1 < z < 0.6$.

The AGN fraction, f_{AGN}, for our sources within these limits is given by

$$f_{AGN} = \sum_{i=0}^{N} \frac{(1 - P^i_{\rm false})(1 - P^i_{\rm XRB})}{N_{\rm total}}\ , \qquad (3)$$

where $P_{\rm false}$ is the false detection probability, $P_{\rm XRB}$ is the XRB probability (see Section 3.2), and $N_{\rm total} = 154$ is the total number of galaxies analyzed with mass $10^9\ M_\odot \leq M_\star \leq 3 \times 10^9\ M_\odot$ and $0.1 < z < 0.6$. All of our $\geq 3\sigma$ sources with luminosity above the incomplete luminosity limit, $L_{\rm X} > 10^{41}$ erg s^{-1}, are included in this calculation. This leaves us with one $\geq 3\sigma$ source (34347), which would indicate an AGN fraction for our $\geq 3\sigma$ sources of 0.6%. However, because of the large uncertainties in this calculation, we can use the $\geq 2\sigma$ sources to provide an upper bound to the AGN fraction. In this case, we have 5 sources within the mass, redshift, and luminosity limits. This gives an AGN fraction for our $\geq 2\sigma$ sources of 3%. Thus, we find an AGN fraction of $\sim 0.6 - 3\%$. This range of fractions are shown in Figure 9.

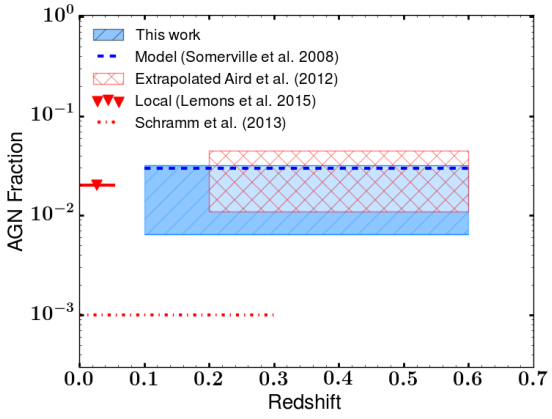

FIG. 9.— AGN Fraction as a function of redshift. The blue, striped region gives our measured AGN fraction for our $\geq 2\sigma$ and $\geq 3\sigma$ sources with $10^9\ M_\odot \leq M_\star \leq 3 \times 10^9\ M_\odot$, $0.1 < z < 0.6$, and $L_{\rm X} \geq 10^{41}$ erg s^{-1}. The blue dashed line gives the AGN fraction found using semi-analytic models and applying the same luminosity and mass cuts. The red, hashed region the AGN fraction range found by extrapolating from Aird et al. (2012) for $10^9\ M_\odot \leq M_\star \leq 3 \times 10^9\ M_\odot$ and $0.2 < z < 0.6$. The red triangle gives the Lemons et al. (2015) AGN fraction.

4.3. *Comparison of Observed & Theoretical AGN Fractions in Dwarf Galaxies*

Several studies have measured AGN fractions for dwarf galaxies in the local universe. It is highly non-trivial to compare our fractions with these other studies, given the different techniques, depths, and redshifts of the different surveys. In an attempt to provide somewhat meaningful comparisons, we here focus on X-ray surveys. Note that most of these studies cross-correlate optical positions of galaxies with an X-ray catalogue rather than performing forced X-ray photometry at the optical positions as we do in this paper. Figure 9 and Table 4 give summaries of these AGN fractions.

Miller et al. (2015) study ~ 200 early-type dwarf galaxies in the local Universe selected optically from *HST* imaging for the AGN Multi-wavelength Survey of Early-type galaxies (AMUSE) surveys (see Gallo et al. 2008; Miller et al. 2012, for details on these surveys). They then use the *Chandra* X-ray Observatory data from the AMUSE survey and Bayesian statistical techniques to study the AGN fraction in galaxies with $M_\star < 10^{10}\ M_\odot$. Miller et al. (2015) report a SMBH occupation fraction of $> 20\%$ down to $L/L_{\rm Edd} \sim 10^{-4}$ for $M_\star < 10^{10}\ M_\odot$. Due to our average sample redshift, we do not probe this low Eddington regime here. Lemons et al. (2015) also focus on the very nearby universe in their survey of dwarf galaxies. They select a sample of $\sim 44,000$ dwarf galaxies from the NASA-Sloan atlas[5] with $z < 0.055$. Lemons et al. (2015) then cross match these sources to the X-ray sources within the *Chandra* Source Catalog. Although they do not give the number of galaxies in the NASA-Sloan atlas that are within the *Chandra* Source Catalog area, we can estimate this number using the relative areas of each of these fields. The SDSS DR7 footprint is $11,663$ deg^2 (Abazajian et al. 2009), and the *Chandra* Source Catalog SDSS observations have an area of 130 deg^2 (Goulding et al. 2014). So, we estimate that of the $\sim 44,000$ dwarf galaxies in the NASA-Sloan atlas Lemons et al. (2015) selected, ~ 491 dwarf galaxies are within the *Chandra* Source Catalog area. Lemons et al. (2015) find 19 dwarf galaxies with hard X-ray detections, although they argue that at most 10 of these are indicative of a central SMBH. This gives an estimated AGN fraction of $\sim 2\%$ for $M_\star < 3 \times 10^9\ M_\odot$ and $z < 0.055$. At somewhat higher redshifts, Schramm et al. (2013) optically select ~ 5200 dwarf galaxies with $M_\star < 3 \times 10^9\ M_\odot$ at $z < 1$ using *HST*/ACS imaging from the Galaxy Evolution from Morphologies and SEDs (GEMS) survey (Rix et al. 2004). They then use multi-wavelength catalogs to match these galaxies to X-ray sources in the *Chandra* Deep Field-South. Schramm et al. (2013) find 27 X-ray detected galaxies among their ~ 5200 dwarf galaxy sample up to $z < 1$. However, they then focus on the sample with $z < 0.3$, optical spectra, and a high ratio of X-ray to optical luminosity, which leaves them with a parent sample of ~ 2100 galaxies and 3 X-ray detected galaxies. They argue that this sample of 3 galaxies all contain AGN by examining their Hα or UV fluxes. Ignoring selection effects, we calculate an AGN fraction of $\sim 0.1\%$. However, Schramm et al. (2013) does not discuss the incompleteness of the sample.

Perhaps the most straightforward comparison is made with the X-ray study of Aird et al. (2012). Aird et al. (2012) select $25,000$ galaxies that are within fields with X-ray data from the PRIMUS survey (Aird et al. 2012). They identify 242 AGN with $L_{\rm X} > 10^{42}$ erg s^{-1} out of this sample using archival *Chandra* and *XMM-Newton* X-ray data. They report an AGN fraction of $\sim 1\%$ up

[5] http://www.nsatlas.org/

to $z \sim 1$ but for more massive galaxies than we consider here. While Aird et al. (2012) focus on different mass ranges than we do here, we can compare to their study because of the central result of that paper: Aird et al. (2012) show that AGN accretion rate distributions do not depend upon the host galaxy stellar mass. They report a universal Eddington ratio for $M_\star > 3 \times 10^9\ M_\odot$ and $L_X > 10^{42}$ erg s^{-1} in the redshift range[6] $z = 0.2 - 0.6$. Given that the AGN accretion rate distribution is independent of the host galaxy stellar mass, we can extrapolate these probability densities to the mass and luminosity ranges we study here. For this linear extrapolation, we use Aird's fit to the figure of active fraction (i.e. probability density of AGN with a given luminosity, L_X in a galaxy of stellar mass, $M_\star$) as a function of AGN X-ray luminosity and stellar mass (Top panels of Figure 4 in Aird et al. 2012). By virtue of the universal accretion rate distribution, we adopt their measured slope (i.e. $P(L_X|M_\star)$ per $\log L_X$ / [erg s^{-1}]) of $\alpha = -0.8$ (Aird et al. 2012). We then use a least squares fit to find the value for the AGN fraction at the 'intercept' ($L_X = 10^{43}$ erg s^{-1}) for $M_\star = 10^9\ M_\odot$, which gives us an intercept of $b = -3.3 \pm 0.3$. Using these values, we calculate the extrapolated AGN fraction for $z = 0.2 - 0.6$ and $M_\star = 10^9\ M_\odot$ (i.e. $P(L_X|M_\star = 10^9\ M_\odot, z = 0.2 - 0.6)$) to be $1.1 - 4.5\%$. This is remarkably consistent with our own results of $0.6 - 3\%$ for $10^9\ M_\odot \leq M_\star \leq 3 \times 10^9\ M_\odot$ and $0.1 < z < 0.6$ (see Figure 9).

We also compare the fractions of detected active black holes with the predictions of a semi-analytic model (SAM) of the joint formation and evolution of galaxies and SMBHs from Somerville et al. (2008) (see also Hirschmann et al. 2012). SAMs are useful tools because they allow us to model a statistical sample down to very low masses, such as those relevant in this paper. The Somerville et al. (2008) models reproduce dwarf galaxy properties well, and manage to match the AGN luminosity function at higher luminosities (Somerville et al. 2012). Thus, it is interesting to ask whether their AGN fractions are similar to ours, with the eventual hope to test their assumptions about seeding and accretion.

The SAM is based on cosmological merger trees and contains recipes for the usual processes included in models of galaxy formation, including gas accretion and cooling, star formation, and stellar feedback. In this model, each top-level halo is seeded with a $10^4\ M_\odot$ black hole. As shown in Hirschmann et al. (2012), these seed masses are required to make the luminous AGN observed at $z > 5$ without resorting to super-Eddington accretion. Black hole accretion is triggered by mergers with mass ratio greater than 1:10, which is based on the results of hydrodynamic simulations of galaxy mergers (Hopkins et al. 2006, 2007). The black hole growth is self-regulated by radiative feedback from the accreting black hole, resulting in a power-law decline of accretion rates as described in Hopkins et al. (2006). Although we consider a SAM in which black hole accretion is triggered only by mergers, in reality, secular processes and internal disk instabilities likely contribute (see Hirschmann et al. 2012). While we exclude visible mergers from our survey, we show in Section 5 that including these mergers would not result in an appreciable change to our results. Moreover, many AGN hosts in the models would not be visually identified as a merger. Many hosts at the accretion levels relevant here had a merger long enough ago that the signatures would no longer be easy to recognize, or were triggered by much smaller objects that would also be difficult to identify in surveys at the present depth.

We select galaxies from a mock AEGIS lightcone using the same stellar mass criteria and redshift range as for the observed sample. Our model predicts the accretion rate onto the black hole, and we convert this to an X-ray luminosity using a conversion of rest mass to energy of 0.1, and the bolometric correction to the hard X-ray band from Marconi et al. (2004). We do not account for obscuration of the AGN radiation. We then compute the AGN fraction by counting the fraction of galaxies in the relevant stellar mass and redshift bins with $L_X \geq 10^{41}$ erg s^{-1}.

In this way, we find a detected AGN fraction for galaxies with stellar mass $10^9\ M_\odot \leq M_\star \leq 3 \times 10^9\ M_\odot$ and in the redshift range $0.1 \leq z \leq 0.6$ of 3.0%, which is encouragingly close to the observational results presented here (see Figure 9). The median Eddington ratio for the active black holes with L_X greater than the detection limit is 3%, while the mean for the same sample is 9%. We have also performed the exercise of adding the X-ray flux expected from high-mass X-ray binaries using Equation 2 at the given stellar masses and SFRs. We find that only a few additional galaxies would be above the adopted X-ray detection limit due to the added contribution to the X-ray flux from HMXBs, resulting in a negligible change in our predicted AGN fractions. This is consistent with the results shown in Figure 6.

While the SAM results agree surprisingly well with the observational results, it is important to understand that significant degeneracy still remains between the Eddington ratio distribution and the occupation fraction. In principle, the scenario that our SAM tests - that of high seed mass and overall low accretion rates - may be correct, in accord with direct gas cloud collapse models (e.g. Eisenstein & Loeb 1995; Regan & Haehnelt 2009; Mayer et al. 2015; Volonteri 2010) or formation in nuclear clusters (e.g. Loeb & Rasio 1994; Goswami et al. 2012; Katz et al. 2015; Stone et al. 2016). On the other hand, there may be a low seed mass and high accretion rates, which agree with Population III star collapse models (e.g. Madau & Rees 2001; Johnson et al. 2012; Becerra et al. 2015). And of course, the truth could be some hybrid of these multiple scenarios. However, the surprising agreement between our observations, the SAM, and the extrapolation from Aird et al. (2012) may suggest that the universal accretion rate distribution does extend to dwarf galaxies. If so, it is most likely that the occupation fraction is of order unity (Miller et al. 2015; Plotkin et al. 2016). We are hopeful that more observational constraints, perhaps from JWST (e.g. Windhorst et al. 2009), will help inform these different scenarios. In addition, further studies similar to our own that focus on a wider mass range of galaxies would be beneficial in truly discerning the AGN fraction as a function of mass. This, combined with the observations from the next-generation telescopes, should allow us to constrain the seeding mechanisms further.

We also use the SAM to predict an AGN fraction for

[6] Note that while Aird et al. (2012) did search to $z < 1$, there were no objects in their lowest mass bin at the higher redshifts.

the same mass and X-ray luminosity limits in the redshift range $z = 1 - 1.5$. We find an AGN fraction in this range of 9.4% and a mean Eddington ratio of 10.3% for the active black holes with X-ray luminosities above the detection limit. This predicted AGN fraction is a bit higher than the one we measure at lower redshifts, which could indicate a rise in AGN activity in dwarf galaxies similar to that in more massive galaxies at higher redshifts. This may be measurable in the near future by next generation surveys.

5. SUMMARY AND FUTURE WORK

Here, we study a sample of 605 dwarf galaxies with the aim of finding AGN and constraining the AGN fraction in these galaxies. First, we identify dwarf galaxies ($M_\star < 3 \times 10^9 M_\odot$) with redshift $z < 1$ using the NEWFIRM Medium-Band Survey, along with *HST* observations and DEEP2 spectra. We then perform aperture photometry using available *Chandra* ACIS-I data at the optical positions of the dwarf galaxies. We identify 10 AGN with $\geq 3\sigma$ certainty and 29 AGN with $\geq 2\sigma$ certainty out of our sample of 605 galaxies. It is difficult to directly separate the emission of high-mass X-ray binaries (HMXBs) from low-luminosity AGN in these galaxies, but we use several different techniques to argue that the majority of our sources are AGN. Most of the hardness ratios of our sources are consistent with AGN rather than HMXBs or X-ray emitting hot gas associated with supernovae remnants, which both have more negative hardness ratios than those we observed. In addition, the L_X we measure is much higher than the estimated X-ray luminosity due to star formation. Also, the number of HMXBs/ULXs in our sample with X-ray luminosities as high as those observed is estimated to be very low. Furthermore, by plotting the optical line ratios found in the DEEP2 spectra of our sources on a BPT diagram, we find that they tend to occupy a region consistent with other AGN.

Finally, we use our results to calculate an AGN fraction for dwarf galaxies - the first time this has been directly calculated beyond the local universe. We find a fraction of $0.6 - 3\%$ for galaxies in the stellar mass range $10^9\ M_\odot \leq M_\star \leq 3 \times 10^9\ M_\odot$ and redshift range $0.1 \leq z \leq 0.6$. This agrees well with other studies, like Lemons et al. (2015) and Schramm et al. (2013), that find the AGN fraction for dwarf galaxies in the nearby universe. It is also consistent with the Aird et al. (2012) universal accretion rate distribution. We also compared our results to semi-analytic models. These models seed all top-level halos with $10^4\ M_\odot$ black holes, and assume that accretion was triggered only by mergers. We find that these results agree well with our observed fraction.

There are some caveats to these results. We exclude ongoing mergers, where the AGN fraction may be higher. We did apply our X-ray analysis to the 43 galaxies that we excluded for being mergers. Of those, we found 2 to have $\geq 3\sigma$ X-ray sources: NMBS IDs 31041($\alpha = 14^h17^m45.674^s$, $\delta = +52°28^m2.29^s$ (J2000)) & 32018 ($\alpha = 14^h18^m19.265^s$, $\delta = +52°33^m51.464^s$ (J2000)). This would increase our $\geq 3\sigma$ AGN fraction to a maximum of $\sim 2\%$. In addition, it is difficult to know the fraction of HMXBs in these galaxies as the effects of metallicity on the HMXB luminosity distribution are still unknown, and these are relatively metal poor systems compared to the galaxies typically studied.

At this point, it is still too early to give any constraints on supermassive black hole seeds. However, it is clear that at least some $\sim 10^9\ M_\odot$ galaxies must have SMBHs. We hope to apply our technique to a larger cosmological volume and over a wider range of masses. In future work, we plan to explore how the predictions of semi-analytic models and numerical hydrodynamic simulations depend on black hole seeding mechanisms, as well as physical mechanisms for the triggering and regulation of black hole growth. This will allow us to properly compare the AGN fractions with other studies, and to give a constraint on seeding mechanisms.

The authors would like to thank the anonymous referee for their very thorough comments. This work is supported by *Chandra* Archival Grant ARX 15700206. K.P. acknowledges support from the National Science Foundation Graduate Research Fellowship Program. Any opinions, findings, and conclusions or recommendations expressed in this material are those of the author(s) and do not necessarily reflect the views of the National Science Foundation. R.S.S. thanks the Downsbrough family for their generous support, and also gratefully acknowledges support from the Simons Foundation in the form of a Simons Investigator grant. R.C.H. acknowledges support from an Alfred P. Sloan Research Fellowship and a Dartmouth Class of 1962 Faculty Fellowship. Support for A.E.R. was provided by NASA through Hubble Fellowship grant HST-HF2-51347.001-A awarded by the Space Telescope Science Institute, which is operated by the Association of Universities for Research in Astronomy, Inc., for NASA, under contract NAS 5-26555. This research has made use of data obtained from the *Chandra* Data Archive, the *Chandra* Source Catalog, and software provided by the *Chandra* X-ray Center (CXC) in the application packages CIAO, ChIPS, and Sherpa.

REFERENCES

Abazajian, K. N., Adelman-McCarthy, J. K., Agüeros, M. A., et al. 2009, ApJS, 182, 543-558
Aird, J., Coil, A. L., Moustakas, J., et al. 2012, ApJ, 746, 90
Baldwin, J. A., Phillips, M. M., & Terlevich, R. 1981, PASP, 93, 5
Barth, A. J., Greene, J. E., & Ho, L. C. 2004, ApJ, 619, 4
Basu-Zych, A. R., Lehmer, B., Fragos, T., et al. 2016, ApJ, 818, 140
Becerra, F., Greif, T. H., Springel, V., & Hernquist, L. E. 2015, MNRAS, 446, 2380
Bellovary, J., Volonteri, M., Governato, F., et al. 2011, ApJ, 742, 13
Bertin, E., & Arnouts, S. 1996, Astron. Astrophys. Suppl. Ser., 117, 393
Brandt, W. N., & Alexander, D. M. 2015, A&A Rev., 23, 1
Brandt, W. N., & Hasinger, G. 2005, ARA&A, 43, 827
Bruzual, G., & Charlot, S. 2003, MNRAS, 344, 1000
Chabrier, G. 2003, PASP, 115, 763
Davis, M., Faber, S. M., Newman, J. a., et al. 2002, Proc. SPIE, 4834, 12
Davis, M., Guhathakurta, P., Konidaris, N. P., et al. 2007, ApJ, 660, L1
den Brok, M., Seth, A. C., Barth, A. J., et al. 2015, ApJ, 801, 16
Desroches, L.-B., & Ho, L. C. 2009, ApJ, 690, 267
Dong, X.-B., Ho, L. C., Yuan, W., et al. 2012, ApJ, 755, 167
Eisenstein, D. J., & Loeb, A. 1995, ApJ, 443, 11
Filippenko, A. V., & Sargent, W. L. W. 1989, ApJ, 342, L11
Fragos, T., Lehmer, B., Tremmel, M., et al. 2013, ApJ, 764, 41

Fruscione, A., McDowell, J. C., Allen, G. E., et al. 2006, Proc. SPIE, 6270
Gallo, E., Treu, T., Jacob, J., et al. 2008, ApJ, 680, 154-168
Gebhardt, K., Lauer, T. R., Kormendy, J., et al. 2001, AJ, 122, 2469
Gibson, R. R., & Brandt, W. N. 2012, ApJ, 746, 54
Gilfanov, M., Grimm, H.-J., & Sunyaev, R. 2004, MNRAS, 347, L57
Goswami, S., Umbreit, S., Bierbaum, M., & Rasio, F. A. 2012, ApJ, 752, 43
Goulding, A. D., & Alexander, D. M. 2009, MNRAS, 398, 1165
Goulding, A. D., Forman, W. R., Hickox, R. C., et al. 2012, ApJS, 202, 26
Goulding, A. D., Forman, W. R., Hickox, R. C., et al. 2014, ApJ, 783, 40
Greene, J. E. 2012, Nat. Commun., 3, 1304
Greene, J. E., & Ho, L. C. 2004, ApJ, 610, 13
—. 2007, ApJ, 13
Greene, J. E., Peng, C. Y., Kuo, C.-Y., et al. 2010, AIP Conf. Proc., 1240, 207
Groves, B. a., Heckman, T. M., & Kauffmann, G. 2006, MNRAS, 371, 1559
Hirschmann, M., Naab, T., Somerville, R. S., Burkert, A., & Oser, L. 2012, MNRAS, 419, 3200
Ho, L. C., Filippenko, A. V., & Sargent, W. L. W. 1997, ApJS, 112, 315
Hopkins, P. F., Lidz, A., Hernquist, L., et al. 2007, ApJ, 662, 110
Hopkins, P. F., Somerville, R. S., Hernquist, L., et al. 2006, ApJ, 652, 864
Johnson, J. L., Whalen, D. J., Fryer, C. L., & Li, H. 2012, ApJ, 750, 66
Kalberla, P. M. W., Burton, W. B., Hartmann, D., et al. 2005, Astron. Astrophys., 440, 775
Katz, H., Sijacki, D., & Haehnelt, M. G. 2015, MNRAS, 451, 2352
Kauffmann, G., Heckman, T. M., Tremonti, C., et al. 2003a, MNRAS, 346, 1055
—. 2003b, MNRAS, 346, 1055
Kewley, L. J., Dopita, M. A., Sutherland, R. S., Heisler, C. A., & Trevena, J. 2001, ApJ, 556, 121
Kormendy, J., & Ho, L. C. 2013, ARA&A, 51, 511
Kriek, M., van Dokkum, P. G., Labbe, I., et al. 2009, ApJ, 221
Laird, E. S., Nandra, K., Georgakakis, A., et al. 2009, ApJS, 180, 102
Lang, D., Hogg, D. W., & Schlegel, D. J. 2014, arXiv:1410.7397
Lehmer, B. D., Alexander, D. M., Bauer, F. E., et al. 2010, ApJ, 559
Lemons, S., Reines, A., Plotkin, R., Gallo, E., & Greene, J. 2015, ApJ, 805, 10
Loeb, A., & Rasio, F. A. 1994, ApJ, 432, 52
Ludwig, R. R., Wills, B., Greene, J. E., & Robinson, E. L. 2009, ApJ, 706, 995
Madau, P., & Rees, M. J. 2001, ApJ, 551, L27
Marconi, A., Risaliti, G., Gilli, R., et al. 2004, MNRAS, 351, 169
Mayer, L., Fiacconi, D., Bonoli, S., et al. 2015, ApJ, 810, 51
McConnell, N. J., Ma, C.-P., Murphy, J. D., et al. 2012, ApJ, 756, 179
Mezcua, M., Civano, F., Fabbiano, G., Miyaji, T., & Marchesi, S. 2016, ApJ, 817, 20
Miller, B., Gallo, E., Treu, T., & Woo, J.-H. 2012, ApJ, 747, 57
Miller, B. P., Gallo, E., Greene, J. E., et al. 2015, ApJ, 799, 98
Mineo, S., Gilfanov, M., & Sunyaev, R. 2012a, MNRAS, 419, 2095
—. 2012b, MNRAS, 426, 1870
Moran, E. C., Shahinyan, K., Sugarman, H. R., Vélez, D. O., & Eracleous, M. 2014, AJ, 148, 136
Moustakas, J., & Kennicutt, Jr., R. C. 2006, ApJS, 164, 81
Nandra, K., Laird, E. S., Adelberger, K., et al. 2005, MNRAS, 356, 568
Nandra, K., Laird, E. S., Aird, J. a., et al. 2015, ApJS, 220, 21
Newman, J. A., Cooper, M. C., Davis, M., et al. 2013, ApJS, 208, 5
Paggi, A., Fabbiano, G., Civano, F., et al. 2015, arXiv:1507.03170
Park, T., Kashyap, V. L., Siemiginowska, A., et al. 2006, ApJ, 652
Plotkin, R. M., Gallo, E., Haardt, F., et al. 2016, arXiv:1605.00742
Regan, J. A., & Haehnelt, M. G. 2009, MNRAS, 393, 858
Reines, A. E., & Deller, A. T. 2012, ApJ, 750, L24
Reines, A. E., Greene, J. E., & Geha, M. 2013, ApJ, 775, 116
Reines, A. E., Plotkin, R. M., Russell, T. D., et al. 2014, ApJ, 787, L30
Reines, A. E., Sivakoff, G. R., Johnson, K. E., & Brogan, C. L. 2011, Nature, 470, 66
Reines, A. E., & Volonteri, M. 2015, ApJ, 813, 82
Rix, H.-W., Barden, M., Beckwith, S. V. W., et al. 2004, ApJS, 152, 163
Sartori, L. F., Schawinski, K., Treister, E., et al. 2015, MNRAS, 454, 3722
Satyapal, S., Böker, T., Mcalpine, W., et al. 2009, ApJ, 704, 439
Satyapal, S., Vega, D., Dudik, R. P., Abel, N. P., & Heckman, T. 2008, ApJ, 677, 17
Schramm, M., Silverman, J. D., Greene, J. E., et al. 2013, ApJ, 773, 150
Seth, A. C., Cappellari, M., Neumayer, N., et al. 2010, ApJ, 714, 713
Somerville, R. S., Hopkins, P. F., Cox, T. J., Robertson, B. E., & Hernquist, L. 2008, MNRAS, 391, 481
Somerville, R. S., Gilmore, R. C., Primack, J. R., & Domínguez, A. 2012, MNRAS, 423, 1992
Steidel, C. C., Adelberger, K. L., Shapley, A. E., et al. 2003, ApJ, 592, 728
Stone, N. C., Kuepper, A. H. W., & Ostriker, J. P. 2016, arXiv:1606.01909
Thornton, C. E., Barth, A. J., Ho, L. C., Rutledge, R. E., & Greene, J. E. 2008, ApJ, 686, 892
Valluri, M., Ferrarese, L., Merritt, D., & Joseph, C. L. 2005, ApJ, 628, 137
van den Bosch, R. C. E., & de Zeeuw, P. T. 2010, MNRAS, 401, 1770
van van Dokkum, P. G., Labbé, I., Marchesini, D., et al. 2009, PASP, 121, 2
Volonteri, M. 2010, ARA&A, 18, 279
Whalen, T. J., Hickox, R. C., Reines, A. E., et al. 2015, ApJ, 806, 37
Whitaker, K. E., Labbe, I., van Dokkum, P. G., et al. 2011, ApJ, 86, 24
Windhorst, R. A., Mather, J., Clampin, M., et al. 2009, astro2010: The Astronomy and Astrophysics Decadal Survey, 2010
Xue, Y. Q., Luo, B., Brandt, W. N., et al. 2016, arXiv:1602.06299

TABLE 1
Basic Properties of $\geq 2\sigma$ Sources

NMBS ID #	α_{J2000}[a] deg	δ_{J2000}[a] deg	z_{spec}[b]	Stellar Mass[c] $\log(M/M_\odot)$	m_K[d] mag	SFR[e] $\log(M_\odot\ \mathrm{yr}^{-1})$	L_{XB}[f] $\log(\mathrm{erg\ s}^{-1})$
1789	214.24665	52.39860	0.2468	9.39	21.2	-1.8	37.43
6614	214.40269	52.49404	0.8105	9.48	23.0	0.28	39.49
7013	214.27524	52.50460	0.8362	9.27	23.1	-0.33	38.88
7290*	214.37594	52.50924	0.1729	9.08	21.3	-0.40	38.81
12516	214.48813	52.61451	0.7601	8.87	23.2	-0.73	38.48
12753	214.61006	52.61919	0.8535	9.41	23.2	-0.060	39.15
13373	214.69795	52.63038	0.3534	8.32	23.9	-2.9	36.35
14021*	214.65990	52.64013	0.2083	9.30	20.7	-1.9	37.33
14708	214.59223	52.65499	0.5818	8.78	23.7	-1.2	38.02
16867	214.79042	52.69311	0.4361	8.95	23.1	-0.34	38.87
16879	214.65076	52.69407	0.4826	9.27	22.8	-0.39	38.82
16986	214.54985	52.69630	0.8427	9.28	23.3	-0.32	38.89
17650*	214.51356	52.70632	0.1789	9.39	19.7	0.47	39.68
18139	214.73561	52.71528	0.7351	9.39	23.0	-1.8	37.42
19869	214.71357	52.74905	0.4409	9.26	22.6	-0.22	38.99
19957*	214.76793	52.75079	0.3545	8.95	22.7	-0.35	38.86
20697	214.86649	52.76676	0.4355	8.62	24.0	-2.5	36.66
20960	214.88444	52.77121	0.4353	8.78	23.6	-0.23	38.98
20987	214.76189	52.77085	0.7380	9.42	22.7	0.010	39.22
21055	214.82581	52.77209	0.2626	8.89	22.0	-0.40	38.81
21091	214.78670	52.77206	0.2650	9.19	21.8	-0.10	39.11
21469	214.86046	52.77822	0.3457	9.00	22.4	-0.11	39.10
21690	214.86846	52.78437	0.7764	9.03	22.7	0.21	39.42
22579	214.90512	52.79933	0.1649	9.22	20.6	-2.0	37.25
24295	214.81801	52.82905	0.7521	9.38	22.7	-0.80	38.41
24680	214.85287	52.83023	0.5774	8.34	23.7	0.30	39.51
30536	214.42972	52.41506	0.7191	9.17	23.5	0.25	39.46
31018	214.49324	52.46432	0.2660	9.35	21.5	-0.30	38.91
31097*†	214.50167	52.47253	0.5321	8.74	24.1	-0.73	38.48
31892	214.33956	52.55662	0.5722	9.41	22.8	0.22	39.43
32364*†	214.52787	52.59865	0.2036	9.42	21.4	-0.42	38.79
32682	214.46519	52.63130	0.1733	8.66	21.9	-0.90	38.31
32708	214.40370	52.63011	0.8414	8.91	24.1	0.18	39.39
32820	214.52603	52.64448	0.2036	9.36	21.7	-0.94	38.27
33817*	214.79648	52.73136	0.08120	8.96	20.8	-0.60	38.61
33865	214.74270	52.73832	0.3836	9.48	21.3	-1.1	38.14
33915*	214.53242	52.73998	0.06730	9.19	20.3	-1.2	38.01
34168*†	214.82505	52.76636	0.3457	8.53	23.1	-1.0	38.18
34347*	214.82049	52.78238	0.4544	9.48	21.9	0.11	39.32

[a] Galaxy positions, as given by the NMBS
[b] Spectroscopic Redshifts, as given by DEEP2
[c] Stellar Mass, as given by the NMBS
[d] Apparent K magnitude, as given by the NMBS
[e] Star Formation Rate, as given by the NMBS
[f] Estimated X-ray Luminosity from XBs, see Section 3.2 for a full description
[*] $\geq 3\sigma$ sources
[†] Position reflects X-ray source position rather than optical position

TABLE 2
X-ray Properties of $\geq 2\sigma$ Sources

ID #	t_{exp} [a] ks	$C_{0.5-2}$ [b]	C_{2-7} [b]	$C_{0.5-7}$ [b]	$F_{0.5-2}$ erg s^{-1}cm^{-2}	F_{2-7} erg s^{-1}cm^{-2}	$F_{0.5-7}$ erg s^{-1}cm^{-2}	HR[c]	$P_{0.5-2}$ [d]	P_{2-7} [d]	$P_{0.5-7}$ [d]	Sig Bands[e]	$P_{\rm XB}$ [f]
1789	153	5^{+3}_{-4}	< 13	9^{+5}_{-6}	$-15.7^{+0.2}_{-0.7}$	< -14.6	$-15.1^{+0.2}_{-0.5}$	$-0.56^{+0.3}_{-0.4}$	0.0746	0.719	0.0416	F	$< 1 \times 10^{-5}$
6614	104	< 14	18^{+10}_{-11}	20^{+12}_{-13}	< -15.0	$-14.3^{+0.2}_{-0.4}$	$-14.6^{+0.2}_{-0.5}$	$0.88^{+0.1}_{-0.2}$	0.789	0.0340	0.0406	H F	$< 1 \times 10^{-5}$
7013	183	5^{+2}_{-2}	1^{+2}_{-3}	6^{+3}_{-4}	$-15.8^{+0.1}_{-0.4}$	$-15.5^{+0.4}$	$-15.4^{+0.2}_{-0.4}$	$-0.53^{+0.3}_{-0.5}$	0.0104	0.304	0.0376	S F	$< 1 \times 10^{-5}$
7290*	195	< 0	6^{+2}_{-2}	4^{+1}_{-2}	< -16.7	$-15.0^{+0.1}_{-0.3}$	$-15.6^{+0.1}_{-0.4}$	$0.96^{+0.04}_{-0.07}$	1.00	9.01×10^{-4}	8.18×10^{-3}	H	0.0120
12516	427	0^{+0}_{-1}	6^{+2}_{-3}	7^{+3}_{-3}	$-17.7^{+0.7}$	$-15.4^{+0.2}_{-0.4}$	$-15.6^{+0.1}_{-0.3}$	$0.88^{+0.1}_{-0.2}$	0.586	0.0249	8.41×10^{-3}	H F	$< 1 \times 10^{-5}$
12753	418	< 0	7^{+3}_{-4}	9^{+3}_{-4}	< -16.9	$-15.3^{+0.2}_{-0.4}$	$-15.5^{+0.1}_{-0.3}$	$0.94^{+0.06}_{-0.1}$	0.918	0.0334	0.0111	H F	$< 1 \times 10^{-5}$
13373	410	10^{+4}_{-5}	< 19	2^{+8}_{-9}	$-15.7^{+0.2}_{-0.4}$	< -14.9	$-16.1^{+0.7}$	$-0.82^{+0.2}_{-0.2}$	0.0223	0.925	0.423	S	$< 1 \times 10^{-5}$
14021*	421	10^{+3}_{-4}	6^{+4}_{-5}	21^{+6}_{-7}	$-15.7^{+0.1}_{-0.2}$	$-15.4^{+0.2}_{-0.9}$	$-15.2^{+0.1}_{-0.2}$	$-0.38^{+0.4}_{-0.2}$	3.53×10^{-4}	0.117	5.58×10^{-4}	S F	$< 1 \times 10^{-5}$
14708	352	2^{+1}_{-2}	4^{+2}_{-3}	7^{+3}_{-4}	$-16.3^{+0.2}_{-0.8}$	$-15.4^{+0.2}_{-0.7}$	$-15.5^{+0.2}_{-0.4}$	$0.25^{+0.6}_{-0.2}$	0.0750	0.0900	0.0279	F	$< 1 \times 10^{-5}$
16867	568	< 22	28^{+15}_{-16}	28^{+17}_{-18}	< -15.5	$-14.8^{+0.2}_{-0.4}$	$-15.2^{+0.2}_{-0.5}$	$0.91^{+0.09}_{-0.1}$	0.835	0.0233	0.0408	H F	$< 1 \times 10^{-5}$
16879	399	10^{+4}_{-5}	6^{+7}_{-8}	14^{+9}_{-10}	$-15.7^{+0.2}_{-0.3}$	$-15.3^{+0.3}$	$-15.3^{+0.2}_{-0.5}$	$-0.30^{+0.4}_{-0.2}$	0.0190	0.227	0.0691	S	$< 1 \times 10^{-5}$
16986	428	< 4	10^{+5}_{-6}	6^{+5}_{-6}	< -16.1	$-15.2^{+0.2}_{-0.4}$	$-15.7^{+0.3}_{-1}$	$0.87^{+0.1}_{-0.2}$	0.636	0.0311	0.141	H	$< 1 \times 10^{-5}$
17650*	409	19^{+4}_{-5}	5^{+4}_{-5}	21^{+6}_{-7}	$-15.4^{+0.09}_{-0.1}$	$-15.4^{+0.3}_{-1}$	$-15.1^{+0.1}_{-0.2}$	$-0.68^{+0.2}_{-0.1}$	$< 1 \times 10^{-5}$	0.140	8.20×10^{-4}	S F	0.124
18139	588	0^{+7}_{-8}	25^{+14}_{-15}	18^{+16}_{-17}	$-16.9^{+0.9}$	$-14.9^{+0.2}_{-0.4}$	$-15.4^{+0.3}_{-1}$	$0.80^{+0.2}_{-0.2}$	0.467	0.0277	0.112	H	$< 1 \times 10^{-5}$
19869	540	< 13	24^{+10}_{-11}	16^{+11}_{-12}	< -15.7	$-14.9^{+0.1}_{-0.3}$	$-15.4^{+0.2}_{-0.6}$	$0.92^{+0.08}_{-0.1}$	0.690	5.51×10^{-3}	0.0754	H	$< 1 \times 10^{-5}$
19957*	688	2^{+3}_{-4}	29^{+8}_{-9}	29^{+10}_{-11}	$-16.6^{+0.4}$	$-14.9^{+0.1}_{-0.2}$	$-15.2^{+0.1}_{-0.2}$	$0.90^{+0.1}_{-0.1}$	0.306	7.50×10^{-5}	1.27×10^{-3}	H F	$< 1 \times 10^{-5}$
20697	639	< 4	13^{+5}_{-6}	13^{+5}_{-6}	< -16.2	$-15.2^{+0.1}_{-0.3}$	$-15.5^{+0.2}_{-0.3}$	$0.92^{+0.08}_{-0.1}$	0.659	6.09×10^{-3}	0.0128	H F	$< 1 \times 10^{-5}$
20960	623	7^{+2}_{-3}	3^{+4}_{-5}	12^{+5}_{-6}	$-16.1^{+0.1}_{-0.3}$	$-15.8^{+0.4}$	$-15.5^{+0.2}_{-0.3}$	$-0.45^{+0.3}_{-0.08}$	8.64×10^{-3}	0.265	0.0144	S F	2.66×10^{-5}
20987	676	2^{+2}_{-3}	11^{+6}_{-7}	8^{+6}_{-7}	$-16.6^{+0.3}$	$-15.3^{+0.2}_{-0.4}$	$-15.8^{+0.3}_{-1}$	$0.68^{+0.3}_{-0.2}$	0.280	0.0340	0.124	H	1.10×10^{-5}
21055	675	6^{+3}_{-3}	< 11	8^{+4}_{-5}	$-16.1^{+0.2}_{-0.4}$	< -15.3	$-15.8^{+0.2}_{-0.5}$	$-0.70^{+0.3}_{-0.3}$	0.0184	0.630	0.0688	S	3.72×10^{-3}
21091	673	6^{+3}_{-3}	< 9	6^{+6}_{-6}	$-16.2^{+0.2}_{-0.5}$	< -15.4	$-15.9^{+0.3}$	$-0.72^{+0.3}_{-0.3}$	0.0409	0.751	0.168	S	0.0418
21469	628	5^{+2}_{-3}	< 8	4^{+4}_{-5}	$-16.2^{+0.2}_{-0.4}$	< -15.4	$-16.0^{+0.3}$	$-0.77^{+0.3}_{-0.2}$	0.0192	0.807	0.181	S	0.0170
21690	710	5^{+2}_{-2}	6^{+3}_{-4}	11^{+4}_{-5}	$-16.3^{+0.1}_{-0.3}$	$-15.6^{+0.2}_{-0.5}$	$-15.7^{+0.1}_{-0.3}$	$0.012^{+0.5}_{-0.4}$	6.33×10^{-3}	0.0479	9.88×10^{-3}	S F	1.59×10^{-5}
22579	682	5^{+2}_{-3}	< 6	3^{+3}_{-4}	$-16.2^{+0.1}_{-0.4}$	< -15.6	$-16.2^{+0.3}$	$-0.82^{+0.2}_{-0.2}$	0.0136	0.865	0.249	S	$< 1 \times 10^{-5}$
24295	713	3^{+1}_{-2}	0^{+1}_{-2}	3^{+2}_{-3}	$-16.5^{+0.1}_{-0.4}$	-17.2^{+1}	$-16.1^{+0.2}_{-0.8}$	$-0.60^{+0.3}_{-0.4}$	9.09×10^{-3}	0.526	0.104	S	$< 1 \times 10^{-5}$
24680	629	3^{+1}_{-2}	< 2	4^{+2}_{-3}	$-16.4^{+0.1}_{-0.4}$	< -16.0	$-16.1^{+0.2}_{-0.7}$	$-0.77^{+0.3}_{-0.2}$	7.97×10^{-3}	0.703	0.0790	S	0.0124
30536	191	1^{+0}_{-1}	1^{+1}_{-1}	4^{+1}_{-2}	$-16.4^{+0.2}$	$-15.7^{+0.2}$	$-15.5^{+0.1}_{-0.4}$	$-0.048^{+0.6}_{-0.4}$	0.123	0.225	9.12×10^{-3}	F	1.76×10^{-5}
31018	161	14^{+7}_{-8}	7^{+13}_{-14}	25^{+16}_{-17}	$-15.2^{+0.2}_{-0.4}$	$-14.9^{+0.5}$	$-14.7^{+0.2}_{-0.5}$	$-0.30^{+0.4}_{-0.2}$	0.0292	0.296	0.0468	S	$< 1 \times 10^{-5}$
31097*	66.3	3^{+1}_{-2}	7^{+2}_{-3}	10^{+2}_{-3}	$-15.5^{+0.1}_{-0.4}$	$-14.4^{+0.1}_{-0.2}$	$-14.7^{+0.1}_{-0.2}$	$0.38^{+0.3}_{-0.3}$	2.15×10^{-3}	4.00×10^{-6}	$< 1 \times 10^{-5}$	S H F	$< 1 \times 10^{-5}$
31892	176	0^{+1}_{-1}	8^{+3}_{-4}	3^{+3}_{-4}	-17.6^{+1}	$-14.9^{+0.1}_{-0.3}$	$-15.6^{+0.3}$	$0.87^{+0.1}_{-0.2}$	0.562	9.78×10^{-3}	0.168	H	2.18×10^{-4}
32364*	425	9^{+2}_{-3}	4^{+2}_{-3}	10^{+3}_{-4}	$-15.8^{+0.1}_{-0.2}$	$-15.5^{+0.2}_{-0.5}$	$-15.5^{+0.1}_{-0.2}$	$-0.39^{+0.4}_{-0.3}$	$< 1 \times 10^{-5}$	0.0420	1.91×10^{-4}	S F	1.68×10^{-3}
32682	379	2^{+1}_{-2}	< 4	2^{+2}_{-3}	$-16.3^{+0.2}_{-0.6}$	< -15.4	$-16.1^{+0.3}$	$-0.59^{+0.3}_{-0.4}$	0.0434	0.690	0.252	S	0.0134
32708	413	5^{+2}_{-3}	1^{+4}_{-5}	6^{+5}_{-6}	$-16.0^{+0.2}_{-0.5}$	$-15.9^{+0.5}$	$-15.6^{+0.3}_{-1}$	$-0.40^{+0.3}_{-0.6}$	0.0430	0.388	0.132	S	$< 1 \times 10^{-5}$
32820	423	1^{+0}_{-1}	1^{+2}_{-3}	7^{+3}_{-3}	$-16.7^{+0.2}$	$-16.1^{+0.4}$	$-15.6^{+0.2}_{-0.3}$	$0.12^{+-0.9}_{-1}$	0.198	0.372	0.0156	F	9.64×10^{-5}
33817*	684	14^{+5}_{-6}	14^{+9}_{-10}	30^{+12}_{-13}	$-15.8^{+0.1}_{-0.2}$	$-15.2^{+0.2}_{-0.5}$	$-15.2^{+0.1}_{-0.2}$	$-0.13^{+0.5}_{-0.3}$	1.99×10^{-3}	0.0594	3.92×10^{-3}	S	0.0318
33865	627	13^{+6}_{-7}	0^{+9}_{-10}	7^{+11}_{-12}	$-15.8^{+0.2}_{-0.3}$	-16.5^{+1}	$-15.8^{+0.4}$	$-0.59^{+0.3}_{-0.4}$	0.0159	0.485	0.272	S	$< 1 \times 10^{-5}$
33915*	398	22^{+5}_{-6}	2^{+7}_{-8}	14^{+9}_{-10}	$-15.4^{+0.1}_{-0.2}$	$-15.8^{+0.6}$	$-15.3^{+0.2}_{-0.5}$	$-0.79^{+0.2}_{-0.2}$	3.00×10^{-6}	0.404	0.0649	S	3.47×10^{-3}
34168*	696	11^{+3}_{-4}	15^{+5}_{-6}	32^{+7}_{-8}	$-15.9^{+0.1}_{-0.2}$	$-15.2^{+0.1}_{-0.2}$	$-15.2^{+0.09}_{-0.1}$	$0.11^{+0.3}_{-0.2}$	3.20×10^{-5}	9.79×10^{-4}	$< 1 \times 10^{-5}$	S H F	$< 1 \times 10^{-5}$
34347*	602	19^{+4}_{-4}	1^{+3}_{-4}	19^{+5}_{-6}	$-15.6^{+0.08}_{-0.1}$	$-16.1^{+0.5}$	$-15.3^{+0.1}_{-0.2}$	$-0.87^{+0.1}_{-0.1}$	$< 1 \times 10^{-5}$	0.360	6.80×10^{-5}	S F	6.77×10^{-5}

[a] Chandra Exposure Time at the Galaxy Position
[b] Net Source Counts in each band
[c] Hardness Ratios, as given by BEHR - see Section 2.2
[d] False Detection Probability for each band - see description in Section 2.2
[e] All Bands in which the source is significant
[f] Probability that the X-ray Luminosity observed could be due to an HXMB - see Section 3.2 for a full description
* $\geq 3\sigma$ sources

TABLE 3
BASIC PROPERTIES OF $\geq 3\sigma$ SOURCES

ID #	α_{J2000} deg	δ_{J2000} deg	z_{spec}	Stellar Mass $\log(M/M_\odot)$	SFR $\log(M_\odot\ yr^{-1})$	L_X[a] $\log(erg\ s^{-1})$	HR[b]	P_{False}[c]	P_{XB}[d]	[NII]/Hα[e]	[OIII]/Hβ[f]
7290	214.37594	52.50924	0.1729	9.08	-0.40	$40.2^{+0.2}_{-0.2}$	$0.96^{+0.04}_{-0.07}$	9.01×10^{-4}	0.0120	-	4.31*
14021	214.65990	52.64013	0.2083	9.30	-1.9	$40.8^{+0.1}_{-0.2}$	$-0.38^{+0.4}_{-0.2}$	5.58×10^{-4}	$< 1 \times 10^{-5}$	-	2.34
17650	214.51356	52.70632	0.1789	9.39	0.47	$40.7^{+0.1}_{-0.2}$	$-0.68^{+0.2}_{-0.1}$	8.20×10^{-4}	0.124	-	3.36
19957	214.76793	52.75079	0.3545	8.95	-0.35	$41.2^{+0.1}_{-0.2}$	$0.90^{+0.1}_{-0.1}$	1.27×10^{-3}	$< 1 \times 10^{-5}$	-	3.71
31097†	214.50167	52.47253	0.5321	8.74	-0.73	$42.1^{+0.1}_{-0.1}$	$0.38^{+0.3}_{-0.3}$	$< 1 \times 10^{-5}$	$< 1 \times 10^{-5}$	0.16	-
32364†	214.52787	52.59865	0.2036	9.42	-0.42	$40.5^{+0.1}_{-0.2}$	$-0.39^{+0.4}_{-0.3}$	1.91×10^{-4}	1.68×10^{-3}	0.47	-
33817	214.79648	52.73136	0.08120	8.96	-0.60	$39.9^{+0.2}_{-0.2}$	$-0.13^{+0.5}_{-0.3}$	1.99×10^{-3}	0.0318	0.29	-
33915	214.53242	52.73998	0.06730	9.19	-1.2	$39.6^{+0.3}_{-0.3}$	$-0.79^{+0.2}_{-0.2}$	$< 1 \times 10^{-5}$	3.47×10^{-3}	.21	-
34168†	214.82505	52.76636	0.3457	8.53	-1.0	$41.2^{+0.1}_{-0.1}$	$0.11^{+0.3}_{-0.2}$	$< 1 \times 10^{-5}$	$< 1 \times 10^{-5}$	0.19	-
34347	214.82049	52.78238	0.4544	9.48	0.11	$41.4^{+0.1}_{-0.1}$	$-0.87^{+0.1}_{-0.1}$	6.80×10^{-5}	6.77×10^{-5}	0.38	-

[a] X-ray Luminosity, as calculated using the net counts in the FB (0.5-7 keV)
[b] Hardness Ratios, as calculated using BEHR
[c] False Detection probability, see Section 2.2 for a full description
[d] Probability the source is a HMXB, see Section 3.2 for a full description
[e] [NII]/Hα Line Ratio from the DEEP2 data
[f] [OIII]/Hβ Line Ratio from the DEEP2 data
* [OIII] from 4959Åline ([OIII]5007Å= 3x[OIII]4959Å)
† Position reflects X-ray source position rather than optical position

TABLE 4
Observed AGN Fractions

Study	Stellar Mass Range $\log(M/M_\odot)$	Redshift Range	AGN Fraction	Parent Galaxy Selection Method
This work	< 9.5	$0.1 - 0.6$	$0.6 - 3\%$	NMBS
Aird et al. (2012)†	< 9.5	0.2 - 0.6	$1.1 - 4.5\%$	PRIMUS
Miller et al. (2015)	< 10	$\lesssim 0.008$	$> 20\%$	Virgo + Field
Schramm et al. (2013)	< 9.5	< 1	$\sim 0.1\%$	GEMS
Lemons et al. (2015)	< 9.5	< 0.055	$\sim 2\%$	NASA-Sloan

† Extrapolated from Aird et al. (2012), as discussed in Section 4.3